

Cyanopolyynes Chemistry around Massive Young Stellar Objects

KOTOMI TANIGUCHI,^{1,2,*} ERIC HERBST,^{1,2} PAOLA CASELLI,³ ALEC PAULIVE,² DOMINIQUE M. MAFFUCCI,² AND MASAO SAITO^{4,5}

¹*Department of Astronomy, University of Virginia, Charlottesville, VA 22904, USA*

²*Department of Chemistry, University of Virginia, Charlottesville, VA 22903, USA*

³*Max-Planck-Institute for Extraterrestrial Physics (MPE), Giessenbachstr. 1, D-85748 Garching, Germany*

⁴*National Astronomical Observatory of Japan (NAOJ), Osawa, Mitaka, Tokyo 181-8588, Japan*

⁵*Department of Astronomical Science, School of Physical Science, SOKENDAI (The Graduate University for Advanced Studies), Osawa, Mitaka, Tokyo 181-8588, Japan*

(Accepted June 26, 2019)

Submitted to ApJ

ABSTRACT

Recent radio astronomical observations have revealed that HC₅N, the second shortest cyanopolyne (HC_{2n+1}N), is abundant around some massive young stellar objects (MYSOs), which is not predicted by classical carbon-chain chemistry. For example, the observed HC₅N abundance toward the G28.28–0.36 MYSO is higher than that in L1527, which is one of the warm carbon chain chemistry (WCCC) sources, by more than one order of magnitude (Taniguchi et al. 2017). In this paper, we present chemical simulations of hot-core models with a warm-up period using the astrochemical code Nautilus. We find that the cyanopolynes are formed initially in the gas phase and accreted onto the bulk and surface of granular ice mantles during the lukewarm phase, which occurs at $25 < T < 100$ K. In slow warm-up period models, the peak abundances occur as the cyanopolynes desorb from dust grains after the temperature rises above 100 K. The lower limits of the abundances of HC₅N, CH₃CCH, and CH₃OH observed in the G28.28–0.36 MYSO can be reproduced in our hot-core models, after their desorption from dust grains. Moreover, previous observations suggested chemical diversity in envelopes around different MYSOs. We discuss possible interpretations of relationships between stages of the star-formation process and such chemical diversity, such as the different warm-up timescales. This timescale depends not only on the mass of central stars but also on the relationship between the size of warm regions and their infall velocity.

Keywords: astrochemistry — ISM: abundances — ISM: molecules — stars: massive

1. INTRODUCTION

Knowledge of the chemical composition allows us to use molecules as powerful diagnostic tools of the physical conditions and dynamical evolution of star-forming regions (e.g., Caselli & Ceccarelli 2012; van Dishoeck 2018). Recent improvements in efficiencies of radio telescopes enable the achievement of high sensitivities with high angular resolution within reasonable observing times. Owing to such developments, we can detect molecules with abundances significantly lower than previously detected species (e.g., McGuire et al. 2018), including isotopologues (Taniguchi et al. 2016a; Taniguchi & Saito 2017; Burkhardt et al. 2018). The discovery of these molecules in various evolutionary stages raises new challenges in the fields of chemical network simulation and laboratory experiment.

Unsaturated carbon-chain species, such as C_{2n}H, CCS, and the cyanopolynes (HC_{2n+1}N), are unique molecules in the interstellar medium. For a long time, they have been thought to be abundant in young starless cores and

decrease in abundance in later stages of low-mass star formation (Benson et al. 1998; Hirota et al. 2009; Suzuki et al. 1992). The precursors of carbon-chain molecules in starless cores are mainly ionic carbon (C^+) and atomic carbon (C). Carbon-chain molecules are mainly formed via gas-phase ion-molecule reactions and neutral-neutral reactions, the reaction rate coefficients of which can be large even at low temperatures such as $T \simeq 10$ K.

In contrast to the above classical picture, low-mass protostellar cores rich in carbon-chain species have been found in sources such as L1527 in Taurus (Sakai et al. 2008) and IRAS15398–3359 in Lupus (Sakai et al. 2009). On the other hand, saturated complex organic molecules (COMs) have been found to be abundant around protostars (Herbst & van Dishoeck 2009) in so-called hot cores and hot corinos in high- and low-mass star-forming regions, respectively. Therefore, the discovery of such low-mass protostellar cores rich in carbon-chain species was surprising initially. The chemistry that produces these species was named “warm carbon chain chemistry” (WCCC; Sakai & Yamamoto 2013). In WCCC, the formation of carbon-chain molecules starts with the desorption of CH_4 from dust grains at a temperature of ~ 25 K. The reaction between CH_4 and C^+ and subsequent gas-phase reactions then lead to the formation of carbon chains (Hassel et al. 2008). The different timescale of prestellar collapse was proposed as an origin of the difference between WCCC and hot corino chemistry (Sakai & Yamamoto 2013); the short and long starless core phases lead to WCCC and hot corino sources, respectively. On the other hand, Spezzano et al. (2016) suggested that different illumination by the interstellar radiation field around dense cloud cores could produce such chemical differentiation, based on their observations toward the L1544 prestellar core. Hence, the origin of the chemical diversity found in low-mass star-forming regions is still controversial.

Observational studies of carbon-chain molecules in high-mass star-forming regions tend to be less detailed than those of low-mass star-forming regions. Nevertheless, cyanopolyynes have been detected in some famous high-mass star-forming regions such as Sgr B2 (Belloche et al. 2013; Bonfand et al. 2017) and the Orion region, Orion KL (Esplugues et al. 2013) and OMC-2 FIR4 (Fontani et al. 2017). Survey observations of HC_3N and HC_5N have been conducted toward high-mass starless cores (HMSCs) and high-mass protostellar objects (HMPOs) using the Nobeyama 45-m radio telescope (Taniguchi et al. 2018c, 2019). This group detected HC_3N in almost all of the target sources and detected HC_5N in half of the HMPOs. Indeed, HC_3N seems to be ubiquitous around HMPOs. Taniguchi et al. (2017) found that HC_5N is abundant in envelopes around three massive young stellar objects (MYSOs) associated with the 6.7 GHz methanol masers using the Green Bank 100-m and Nobeyama 45-m telescopes. The HC_5N abundance in G28.28–0.36, which is one of the target MYSOs, is higher than that in the Class 0 protostar L1527 by a factor of 20. In addition, Taniguchi et al. (2018b) suggested chemical diversity around MYSOs as a reason for the varying cyanopolyne abundances; organic-poor MYSOs are surrounded by a cyanopolyne-rich lukewarm envelope, while organic-rich MYSOs, namely hot cores, are surrounded by a CH_3OH -rich lukewarm envelope.

In this paper, we report an investigation of the cyanopolyne chemistry using hot-core models with a warm-up period, motivated by the particularly high abundance of HC_5N in the G28.28–0.36 MYSO. Cyanopolyynes are relatively stable species compared with other carbon-chain species and can survive in high temperature regions (Hassel et al. 2011). In fact, the vibrationally excited lines of HC_3N and the extremely high- J rotational lines of HC_5N have been detected in Sgr B2(N) and Orion KL (Bonfand et al. 2017; Esplugues et al. 2013). In addition, HC_3N and HC_5N were detected in a candidate position of the molecular outflow around G28.28–0.36 (Taniguchi et al. 2018a). Therefore, there is a large possibility that cyanopolyynes exist in hot core regions, where the temperature is higher than in WCCC sources, and where formation mechanisms of cyanopolyynes may differ in the two types of regions. Furthermore, the formation paths of cyanopolyynes have been thought to consist of possible steps in the synthesis of prebiotic molecules (Jaber Al-Edhari et al. 2017), so it is also important to reveal their formation paths for science related to the origins of life.

In Section 2, we describe our models, with results found in Section 3. We compare models, and the model results with the observational results around MYSOs (Taniguchi et al. 2017, 2018b) in Sections 4.1 and 4.2, respectively. Effects of the cosmic-ray ionization rate on the HC_5N abundance are investigated in Section 4.3. The chemistry of cyanopolyynes is compared with that of other carbon-chain species during the warm-up period in Section 4.4. Possible origins of the chemical diversity around MYSOs are discussed in Section 4.5. Finally, our conclusions are presented in Section 5.

2. MODELS

In this study, we used the gas-grain Nautilus code (Ruaud et al. 2016) supplemented by preliminary reactions involving irradiation (Shingledecker & Herbst 2018) to model the free-fall collapse and warm-up periods of hot core

Table 1. Initial elemental abundances with respect to total Hydrogen

Element	Abundance
H ₂	0.5
He	0.09
C ⁺	7.3×10^{-5}
N	2.14×10^{-5}
O	1.76×10^{-4}
F	1.8×10^{-8}
Si ⁺	8×10^{-9}
S ⁺	8×10^{-8}
Fe ⁺	3×10^{-9}
Na ⁺	2×10^{-9}
Mg ⁺	7×10^{-9}
Cl ⁺	1×10^{-7}
P ⁺	2×10^{-10}

NOTE—Taken from the AL model in Acharyya & Herbst (2017).

evolution (Garrod & Herbst 2006). We ran both the three-phase model, in which the chemistry of the grain surface and the bulk ice are distinguished, and the two-phase model, in which the grain surface and bulk ice are not distinguished (Ruaud et al. 2016). The cosmic-ray ionization rate was assumed to be $1.3 \times 10^{-17} \text{ s}^{-1}$. The ratio between diffusion energy and binding energy was set at 0.5 (Garrod & Herbst 2006). The binding energies of major species and key species in the following sections are summarized in Appendix A. The competitive mechanism was used for surface reactions with chemical activation energy (Herbst & Millar 2008). Table 1 lists the initial elemental abundances with respect to total hydrogen. These elemental abundances correspond to the low-metal abundances, which are typically used for modeling the chemistry of dark clouds. We assume that all of hydrogen is in the form of H₂ at the initial stage. There are 7646 gas-phase reactions and 498 gas-phase species, mainly taken from the Kinetic Database for Astrochemistry (KIDA)¹. We also included data taken from Balucani et al. (2015) and Skouteris et al. (2018). Balucani et al. (2015) proposed the new formation reactions forming methyl formate and dimethyl ether. Skouteris et al. (2018) studied a new scheme for the synthesis of glycolaldehyde, acetic acid, and formic acid. There are 5323 grain-surface reactions and 431 grain-surface species including suprathreshold species (Shingledecker & Herbst 2018). The surface reactions come mainly from Garrod (2013), with additional data taken from Bergantini et al. (2018) and Hudson & Moore (2018). The reactions between CH₃OH and CH₂^{*} (the asterisk mark (*) means the suprathreshold species; Bergantini et al. 2018) and between CH₃CO and CH₃ including suprathreshold species (Hudson & Moore 2018; Shingledecker & Herbst 2018) are included. The self-shielding effects of H₂ (Lee et al. 1996), CO (Visser et al. 2009), and N₂ (Li et al. 2013) are included.

In addition to the self-shielding effects, Nautilus allows for variation of different parameters through switches. Included switches are as follows: enhancement of H₂ grain formation (off); enabling of photodesorption of ices (on); inclusion of cosmic-ray diffusion (on)²; inclusion of Eley-Rideal mechanism (off); enabling of radiolysis (off). In our reaction network, reactions between cyanopolyynes and radicals on dust surface, which lead to destruction of cyanopolyynes, are not included. Since few of these processes have been studied to the best of our knowledge, and since theoretical treatments are not readily available, we did not try to add such reactions to our network. As shown in the following sections, cyanopolyynes in the gas-phase are destroyed mainly by atomic and molecular ions, which are not included in dust surface and ice mantles: all dust-surface and ice-mantle species are neutral. One neutral species,

¹ <http://kida.obs.u-bordeaux1.fr>

² The effect of cosmic ray impacts which cause a stochastic heating of the dust particles allowing for surface radicals to diffuse quickly and react to form more complex species (Reboussin et al. 2014).

Table 2. Summary of models

Model	t_h ^a	phase
M1	Fast	3 phase
M2	Medium	3 phase
M3	Slow	3 phase
M4	Fast	2 phase
M5	Medium	2 phase
M6	Slow	2 phase

^a Fast, Medium, Slow correspond to 5×10^4 , 2×10^5 , and 1×10^6 yr, respectively.

which can destroy the cyanopolyynes, is neutral atomic carbon, but its abundance on dust surfaces is rather low due to rapid hydrogenation reactions even at low temperatures.

We adopted the physical evolution of the two-stage hot-core model described by Garrod & Herbst (2006). The first stage corresponds to the free-fall collapse period. The initial gas density is $n_H = 10^4 \text{ cm}^{-3}$ and increases to 10^7 cm^{-3} during the free-fall collapse, which lasts for $\sim 5 \times 10^5 \text{ yr}$, while the visual extinction (A_V) increases from 5 mag to over 500 mag according to the increase in n_H . The temperature is kept constant at 10 K (Garrod & Herbst 2006).

The second stage is the warm-up period, during which the temperature rises from 10 K to 200 K according to the following formula (Garrod & Herbst 2006):

$$T = T_0 + (T_{\max} - T_0) \left(\frac{\Delta t}{t_h} \right)^n, \quad (1)$$

where T_0 , T_{\max} , t_h , and n are the initial temperature (10 K), the maximum temperature (200 K), the heating timescale, and the order of the heating, respectively. We chose $n = 2$, following Hassel et al. (2008). Three heating timescales were adopted: $5 \times 10^4 \text{ yr}$ (Fast), $2 \times 10^5 \text{ yr}$ (Medium), and $1 \times 10^6 \text{ yr}$ (Slow), approximating high-mass, intermediate-mass, and low-mass star-formation, respectively (Viti et al. 2004). The dust temperature is assumed to be equal to the gas temperature. Figure 1 shows the time variation of temperature, H_2 density, and visual extinction. After the final temperature of 200 K is reached, the system remains at this temperature, at which chemistry can still occur. In practice, several dynamical changes such as the molecular outflow and disk formation occur, but our models do not include the effects from these phenomena. Table 2 summarizes the models utilized.

3. RESULTS

3.1. Cyanopolyne Chemistry during the Free-Fall Collapse Period

Figure 2 shows the abundances of HC_3N , HC_5N , and HC_7N in the gas phase during the free-fall collapse period. The abundances of HC_3N and HC_5N at time scales of $5 \times 10^3 - 4 \times 10^5 \text{ yr}$ agree with the abundances observed in high-mass starless cores ($X(\text{HC}_3\text{N}) \sim 10^{-11} - 10^{-10}$ and $X(\text{HC}_5\text{N}) \sim 10^{-12} - 10^{-11}$; Taniguchi et al. 2018c). High-mass starless cores typically have gas densities of order 10^4 cm^{-3} at fractions of a parsec (Beuther et al. 2002). Therefore, the results during the free-fall collapse period seem to be reasonable.

During the free-fall collapse stage, the following reaction significantly contributes to the formation of HC_3N ;



After an interval of $6 \times 10^3 \text{ yr}$, HC_3N is also formed significantly by the dissociative recombination reaction



Several reactions contribute to the formation of HC_5N and HC_7N , and their fraction changes with time. The following types of reactions largely form these species:



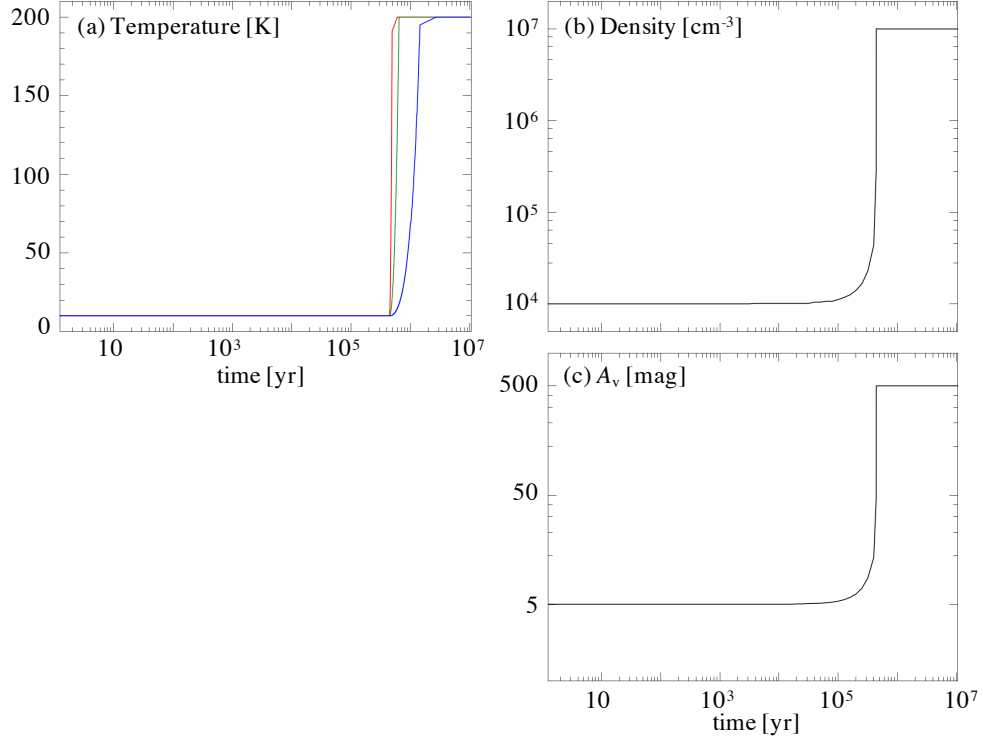


Figure 1. Time variations of (a) temperature, (b) H_2 density, and (c) visual extinction, respectively. In panel (a), red, green, and blue lines indicate the heating timescales of the Fast, Medium, and Slow warm-ups, respectively. In the other panels, the slow model was utilized.

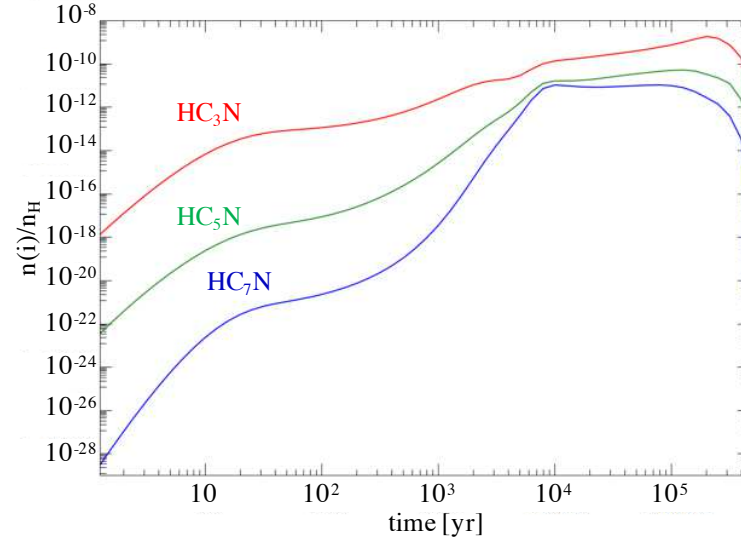


Figure 2. Cyanopolyne's abundances in the gas phase during the free-fall collapse period. The red, green, and blue lines indicate HC_3N , HC_5N , and HC_7N , respectively.



and



where $n = 5, 7$.

Cyanopolyynes are mainly destroyed by reactions with C^+ before 5×10^3 yr and reactions with C between 5×10^3 and 2×10^5 yr:



and



where $n = 3, 5, 7$.

3.2. Cyanopolyne Chemistry during the Warm-up period

Figure 3 shows cyanopolyne abundances in the gas phase, dust surface, and bulk of the icy mantle during the warm-up period for the slow, three-phase model M3. The zero of time is the starting time of the model calculation in the free-fall collapse stage. The left-hand side of each abscissa corresponds to the start of the warm-up period, at around 5×10^5 yr. Note that the temperature is followed with time by a black dashed line. The formation mechanisms of cyanopolyynes are basically the same in all of the models, depending on the temperature. We use Model M3 because we can investigate the temperature dependence of cyanopolyne chemistry during the warm-up period in most detail.

3.2.1. HC_3N

The HC_3N abundance, especially in the gas phase, begins an increase around $t = 7 \times 10^5$ yr when the temperature reaches 25 K and the WCCC chemistry onsets (Sakai & Yamamoto 2013). Figure 4 shows the CH_4 abundances in the gas phase, dust surface, and bulk of the icy mantle of Models M3 and M6. The gas-phase CH_4 abundance steeply increases and the abundances in dust surface and ice mantles decrease at $t = 7 \times 10^5$ yr. At that time, methane (CH_4) desorbs into the gas phase from the dust surface, and then CH_4 reacts with C^+ leading to the formation of C_2H_2 via the electron recombination reactions involving $C_2H_3^+$ and $C_2H_4^+$ (Hassel et al. 2008). The C^+ ion is formed by the reaction between CO and He^+ . C_2H_2 reacts with CN to form HC_3N :



This reaction was suggested as the main formation pathway of HC_3N based on observations of its three ^{13}C isotopologues toward the G28.28–0.36 MYSO (Taniguchi et al. 2016b). Therefore, our model result and the observational result reach the same conclusion. Small subsequent peaks in the HC_3N gaseous abundance correspond to an enhancement in Reaction (10), which relates to both the CN and C_2H_2 abundances. For example, the CN abundance sharply increases due to its direct desorption from dust grains around $t = 7.7 \times 10^5$ yr ($T \simeq 31$ K). Around $t = 9.3 \times 10^5$ yr ($T \simeq 55$ K), the gas-phase C_2H_2 abundance increases because of its desorption from dust grains. The increases in the gas phase values of CN and C_2H_2 lead to separate enhancements in the HC_3N gas phase abundance through Reaction (10).

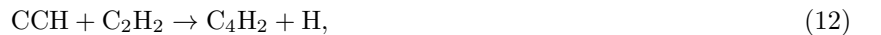
At these low temperatures, HC_3N formed in the gas phase is partially depleted onto dust grains following each enhancement and accumulates in the bulk of the icy mantle. The result is a pattern for the HC_3N abundance vs time that resembles a spectrum. At $t \simeq 1.1 \times 10^6$ yr ($T \simeq 90$ K), HC_3N sublimates from dust grains and reaches its peak abundance in the gas phase. The peak abundance in the gas phase is consistent with that of the bulk of the icy mantle, as shown in panel (a) of Figure 3.

3.2.2. HC_5N

HC_5N is mainly formed by the following reaction in the warming gas ($T > 25$ K):



while the precursor C_4H_2 is produced by the reaction



and the radical CCH is formed by the electron recombination reaction of $C_2H_3^+$. The ion $C_2H_3^+$ is formed by the reaction between CH_4 and C^+ , as discussed in the preceding section. The gas-phase species C_4H_2 sharply increases at

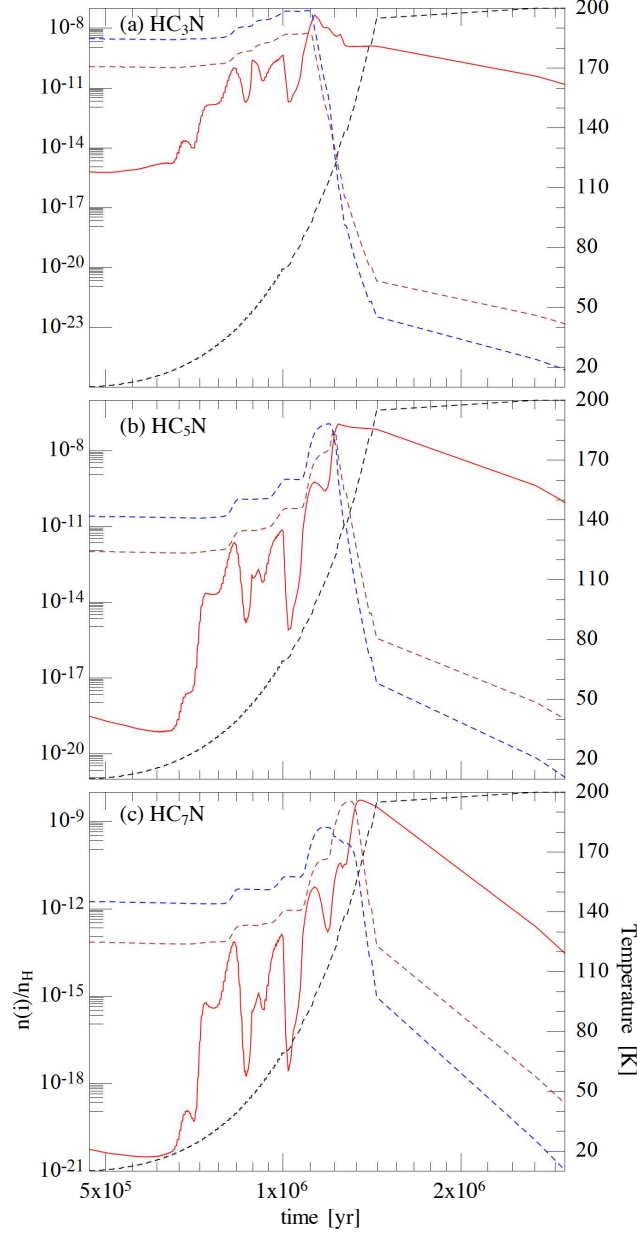


Figure 3. Cyanopolyne abundances during the warm-up period of the slow three-phase model (Model M3). Panels (a), (b), and (c) show the results for HC_3N , HC_5N , and HC_7N , respectively. The red solid line, brown dashed line, and blue dashed line indicate abundances in the gas phase, dust surface, and bulk of the icy mantle, respectively. The black dashed lines indicate temperature.

$t = 1.0 \times 10^6$ yr ($T \simeq 73$ K) via its direct sublimation from dust grains. Owing to increases in the C_4H_2 abundance, Reaction (11) is enhanced, leading to an increase in the HC_5N abundance. The radical CCH also reacts with HC_3N in the gas phase to produce HC_5N by the reaction



The species HC_5N formed in the gas phase is partially accreted into the bulk of the icy mantle, as is the case for HC_3N . At $t = 1.2 \times 10^6$ yr ($T \simeq 115$ K), HC_5N is desorbed into the gas, and reaches its peak abundance. This abundance corresponds to that in the bulk of the mantle, right before desorption, as shown in panel (b) of Figure 3, in a similar manner to HC_3N . The subsequent decrease is caused by reaction with HCO^+ and other protonated ions.

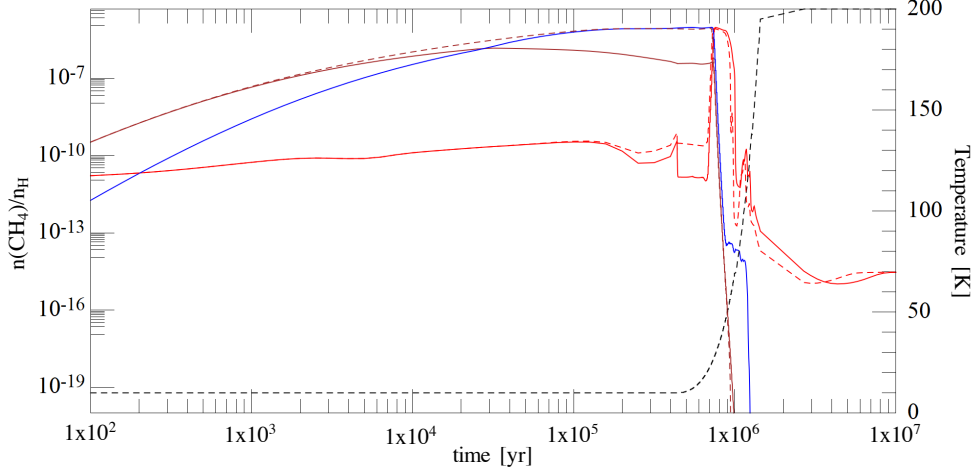


Figure 4. Methane (CH_4) abundances of the slow three-phase model (Model M3) and two-phase model (Model 6) during the free-fall and warm-up periods. The solid and dashed lines show the results of Model M3 and M6, respectively. The red, brown, and blue lines indicate abundances in the gas phase, dust surface, and bulk of the icy mantle, respectively. The abundance in the bulk of the icy mantle is plotted only for Model M3. The black dashed lines indicate temperature.

3.2.3. HC_7N

After the temperature reaches 25 K, HC_7N is efficiently formed by the following reaction:



The C_6H_2 species is formed by the reaction between CCH and C_4H_2 , which is similar to Reaction (12). In addition, gaseous C_6H_2 reaches its peak abundance just after its direct sublimation from dust grains at $t = 1.2 \times 10^6$ yr ($T \simeq 94$ K) and the reaction rate of Reaction (14) increases. This leads to an increase in the HC_7N abundance. The HC_7N species is also produced by the reaction



Analogously to the cases of HC_3N and HC_5N , HC_7N also accumulates on the dust surface and in the bulk of the icy mantle and is desorbed into the gas phase around $t = 1.3 \times 10^6$ yr ($T \simeq 145$ K). The peak abundance of HC_7N in the gas phase is comparable to that on the dust surface, not in the bulk of the icy mantle, as shown in panel (c) of Figure 3.

Besides adsorption onto dust grains, cyanopolynes are efficiently destroyed by the reactions with HCO^+ and other ions during the warm-up period:



where $n = 3, 5, 7$.

The peak abundance of HC_5N is higher than that of HC_3N , which may not be realistic. Occasionally the largest species in a sequence, such as HC_7N (if it is truly the largest) is not described well in a network. The high HC_5N abundance may reflect that there are unknown important destruction reactions of cyanopolynes both in the gas phase and dust surface. For example, radicals can move on dust grains during the warm-up period and reactions between cyanopolynes and radicals may decrease the abundances of cyanopolynes on dust surface and ice mantles. However, our current reaction networks does not contain such reactions, while photodissociation destruction processes are included. Besides photodissociation processes, if other destruction reactions of cyanopolynes on dust surface exist, the longer cyanopolynes will be more affected because longer cyanopolynes stay longer time due to higher sublimation temperatures in our current model.

In summary, the cyanopolynes are produced by a combination of neutral-neutral and ion-neutral gas-phase reactions during the warm-up period ($T > 25$ K) and accumulate on and in the dust mantles before the temperature reaches their sublimation temperatures. The sublimation of first CN and secondly the C_{2n}H_2 ($n = 1, 2, 3$) species enhances key reactions to form the cyanopolynes, which partly accrete onto dust mantles. As the temperature rises, the pattern of enhancements in the production of the gaseous cyanopolynes followed by partial accretion onto grains leads to a characteristic spectral-type pattern. When the temperature rises past the sublimation temperatures of cyanopolynes,

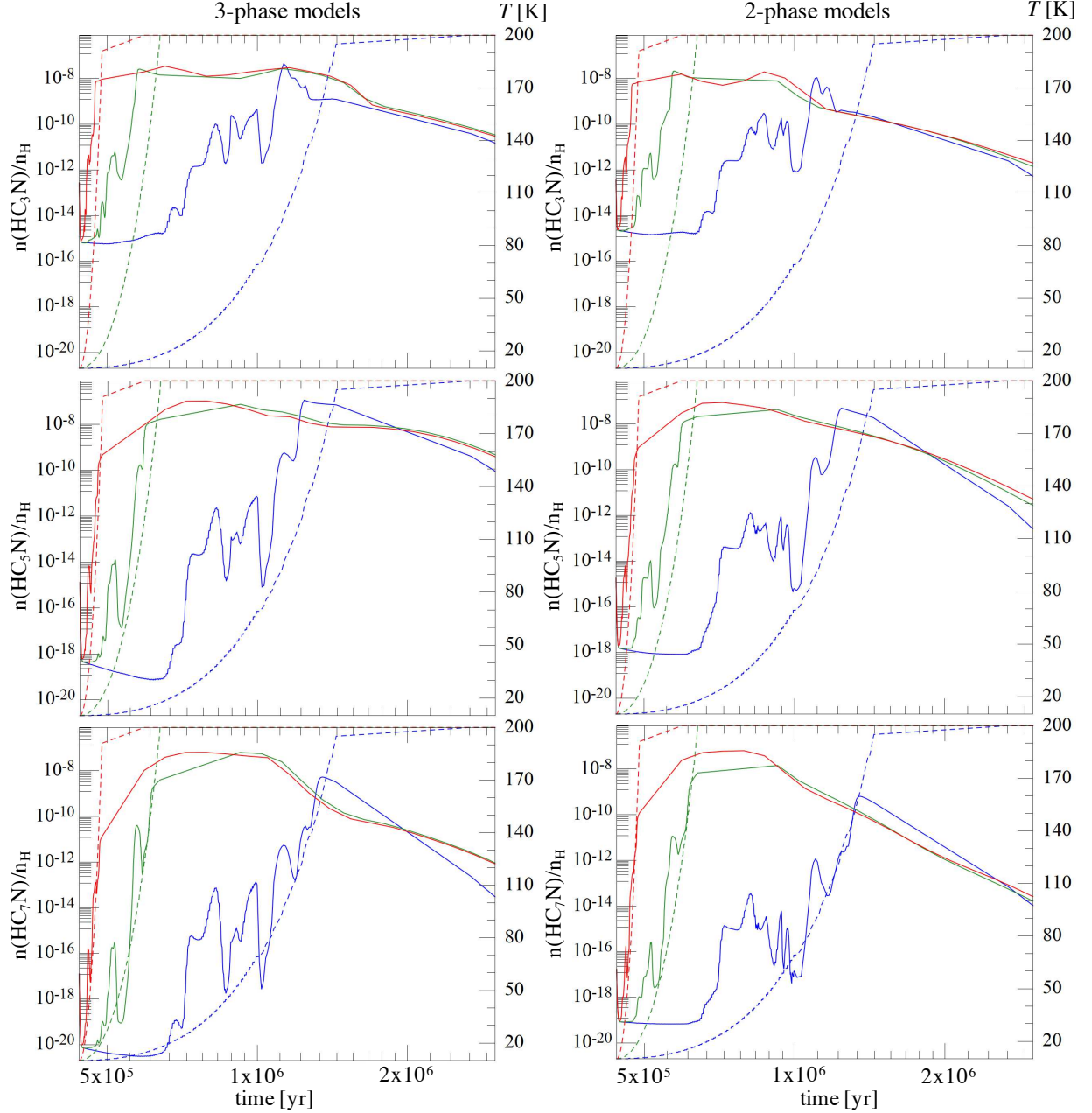


Figure 5. Comparisons of gas-phase cyanopolyne abundances in the warm-up period among models. The upper, middle, and lower panels show results of HC_3N , HC_5N , and HC_7N , respectively. The different colors of lines indicate different heating timescales; red, green, and blue indicate Fast, Medium, and Slow, respectively. The dashed lines indicate the temperature and their colors correspond to the heating timescales. The left panels show the 3-phase models (M1 – M3) and right panels show the 2-phase models (M4 – M6).

they desorb into the gas, and reach their peak abundances. The spectral-type abundance profile is best seen in the slow models, but exists to a lesser extent in the faster models too. Cyanopolyynes are mainly destroyed by reactions with HCO^+ and other protonated ions in the gas phase and their abundances decrease.

4. DISCUSSION

4.1. Comparisons of Cyanopolyne Abundances among Models

Table 3. The peak calculated abundances of cyanopolyynes in the gas phase and the corresponding temperature

Model	HC ₃ N		HC ₅ N		HC ₇ N	
	Abundance	<i>T</i> (K)	Abundance	<i>T</i> (K)	Abundance	<i>T</i> (K)
M1	3.62×10^{-8}	200	1.08×10^{-7}	200	6.03×10^{-8}	200
M2	2.79×10^{-8}	200	7.66×10^{-8}	200	6.20×10^{-8}	200
M3	4.39×10^{-8}	98	1.14×10^{-7}	129	5.19×10^{-9}	162
M4	1.98×10^{-8}	200	8.97×10^{-8}	200	6.41×10^{-8}	200
M5	2.15×10^{-8}	96	4.42×10^{-8}	200	1.45×10^{-8}	200
M6	1.11×10^{-8}	92	5.02×10^{-8}	129	6.44×10^{-10}	162

Figure 5 shows comparisons of the cyanopolyne abundances in the gas-phase during the warm-up period, among all models, while Table 3 summarizes the peak abundances during the warm-up and hot-core periods of cyanopolyynes in the gas phase and the corresponding temperatures in each model. In the fast and medium warm-up models (red and green lines), cyanopolyynes reach higher abundances in the gas phase after their desorption. Given the rapidity of desorption, their peak abundances do not correspond to their abundances on the dust surface or bulk of the icy mantle during the desorption. The post-desorption syntheses in the gas phase are particularly important for the longer chains. One possible reason for their importance is that there is not enough time to accumulate on dust surfaces or in the bulk of the icy mantles during the short heating timescale. On the other hand, accumulation on dust surface and in the bulk of the icy mantle play essential roles in producing the high cyanopolyne abundances during the warm-up period when there is enough time for cyanopolyynes to adsorb onto dust grains. This seems to depend on the assumed initial density.

When we compare the peak abundances in Model M3 (slow; 3-phase) with those in Model M6 (slow, 2-phase), we find that the peak abundances in M3 are higher by a factor of 2 – 8, as shown in Table 3. These different peak abundances between Models M3 and M6 support the hypothesis that accumulation of cyanopolyynes in the bulk of the icy mantle enhances their abundances in the gas phase after their desorption at higher temperatures, because, basically, the ice prevents the gas phase destruction of cyanopolyynes by maintaining their peak abundances unaltered in the mantles.

4.2. Comparisons with Observations

Table 4 contains summaries of the observed abundances of HC₅N, CH₃CCH, and CH₃OH in three MYSOs (Taniguchi et al. 2017, 2018b) and the peak calculated abundances in each model. We excluded HC₃N because its column densities and excitation temperatures in the observed MYSOs seem to include large uncertainties (Taniguchi et al. 2018b). These observations were carried out using single-dish telescopes and thus, because of beam dilution, the derived abundances and rotational temperatures are lower limits (Taniguchi et al. 2017). Hence, our criterion for reproduction is that the model produces more than the observed lower limit in the following sections.

We found that the maximum model abundances of the three gas-phase species are higher than the observed lower limits in all of the models. We also derived their abundances in L1527, a low-mass WCCC source, and found, once again that the model peak abundances exceed the observed lower limits.

We are particularly interested in G28.28–0.36, because this source shows a uniquely high HC₅N/CH₃OH feature, discussed below, among the observed sources (Taniguchi et al. 2018b). In addition, G28.28–0.36 shows a relatively high HC₅N abundance, as derived with the single-dish observations (Taniguchi et al. 2017). In the Orion KL hot core, the HC₅N abundance with respect to H₂ was derived to be 1.7×10^{-10} (Esplugues et al. 2013). Therefore, the HC₅N abundance in G28.28–0.36 is higher than that in the Orion KL hot core by more than one order of magnitude. As already mentioned in Section 1, the HC₅N abundance in G28.28–0.36 is higher than that in L1527 by a factor of 20, as shown in Table 4. The particularly high HC₅N abundance in G28.28–0.36 cannot be explained by warm carbon-chain chemistry (WCCC) in the lukewarm envelope ($T \sim 20 - 30$ K, Hassel et al. 2008, 2011).

We now compare our model results with the lower limits of HC₅N, CH₃CCH, and CH₃OH in G28.28–0.36 in order to constrain the minimum temperatures in the warm-up period where they reside. Figure 6 shows the model results with the lower limits to molecular abundances in G28.28–0.36 as horizontal black dashed lines. Table 5 summarizes

Table 4. Lower limits of observed abundances in MYSOs and the peak calculated abundances of HC₅N, CH₃CCH, and CH₃OH

Source/Model	HC ₅ N	CH ₃ CCH	CH ₃ OH
<i>Observation^a</i>			
G12.89+0.49	$5.0^{+3.1}_{-2.7} \times 10^{-10}$	$2.1^{+1.4}_{-1.1} \times 10^{-8}$	$6.0^{+9.0}_{-4.5} \times 10^{-8}$
G16.86−2.16	$(8.0 \pm 3.5) \times 10^{-10}$	$1.6^{+0.95}_{-0.75} \times 10^{-8}$	$4.4^{+5.5}_{-2.9} \times 10^{-8}$
G28.28−0.36	$2.1^{+1.3}_{-1.0} \times 10^{-9}$	$3.8^{+2.6}_{-2.2} \times 10^{-8}$	$2.3^{+3.5}_{-1.7} \times 10^{-8}$
L1527 (WCCC) ^b	$(1.2 \pm 0.3) \times 10^{-10}$	$(1.07 \pm 0.05) \times 10^{-9}$	$(1.1 \pm 0.2) \times 10^{-9}$
<i>Model</i>			
M1	1.08×10^{-7}	9.27×10^{-7}	6.32×10^{-6}
M2	7.66×10^{-8}	9.23×10^{-7}	4.76×10^{-6}
M3	1.14×10^{-7}	2.42×10^{-7}	9.66×10^{-8}
M4	8.97×10^{-8}	9.61×10^{-7}	3.60×10^{-6}
M5	4.42×10^{-8}	9.03×10^{-7}	3.02×10^{-6}
M6	5.02×10^{-8}	2.80×10^{-7}	6.46×10^{-8}

^a Abundances taken from Taniguchi et al. (2017, 2018b) and converted to abundances with respect to total hydrogen.

^b Column densities of HC₅N, CH₃CCH, and CH₃OH taken from Sakai & Yamamoto (2013) and $N(\text{H}_2)$ value of $2.8 \times 10^{22} \text{ cm}^{-2}$ taken from Jørgensen et al. (2002). The abundances with respect to H₂ are converted to abundances with respect to total hydrogen.

Table 5. The range of age and lower limit of temperature constrained by comparisons with the observational results in G28.28−0.36

Model	Age (yr)			Lower limit of temperature (K)		
	HC ₅ N	CH ₃ CCH	CH ₃ OH	HC ₅ N	CH ₃ CCH	CH ₃ OH
M1	$5.94 \times 10^5 - 2.48 \times 10^6$	$4.71 \times 10^5 - 7.19 \times 10^5$	$4.75 \times 10^5 - 7.19 \times 10^5$	200	84	100
M2	$5.92 \times 10^5 - 2.64 \times 10^6$	$5.64 \times 10^5 - 6.39 \times 10^5$	$5.79 \times 10^5 - 6.39 \times 10^5$	120	84	100
M3	$1.21 \times 10^6 - 1.44 \times 10^6$	$1.07 \times 10^6 - 1.16 \times 10^6$	$1.16 \times 10^6 - 1.19 \times 10^6$	118	82	105
M4	$5.94 \times 10^5 - 1.70 \times 10^6$	$4.70 \times 10^5 - 5.94 \times 10^5$	$4.74 \times 10^5 - 5.94 \times 10^5$	200	78	98
M5	$5.90 \times 10^5 - 1.64 \times 10^6$	$5.59 \times 10^5 - 6.39 \times 10^5$	$5.74 \times 10^5 - 6.39 \times 10^5$	118	78	96
M6	$1.19 \times 10^6 - 1.44 \times 10^6$	$1.05 \times 10^6 - 1.12 \times 10^6$	$1.13 \times 10^6 - 1.17 \times 10^6$	112	78	98

the range of ages and lower limits of temperature constrained by the comparisons between the model results and the observed lower limits. The range of ages is determined as the continuous times when the model abundances are higher than the observed lower limits.

The observed lower limit of HC₅N is reproduced only at ages after it desorbs from dust grains in all the models. Therefore, the chemistry in the lukewarm temperature range of $25 < T < 100$ K cannot explain the high HC₅N abundance in G28.28−0.36, because its desorption temperature is higher than 100 K. The ages when the temperature reaches at the HC₅N sublimation temperature of ~ 115 K are 5.9×10^5 yr and 1.2×10^6 yr in the Medium and Slow warm-up models, respectively. In the Fast warm-up models, further gas-phase formation is needed to reproduce the observed HC₅N abundance. Hence, the lower limit of the observed HC₅N abundance cannot be reproduced at its sublimation temperature ($t \sim 4.8 \times 10^5$ yr).

The carbon-chain species CH₃CCH, shown in the middle panels of Figure 6, is formed in the gas phase during the warm-up period triggered initially by desorption of CH₄ via the following reactions:



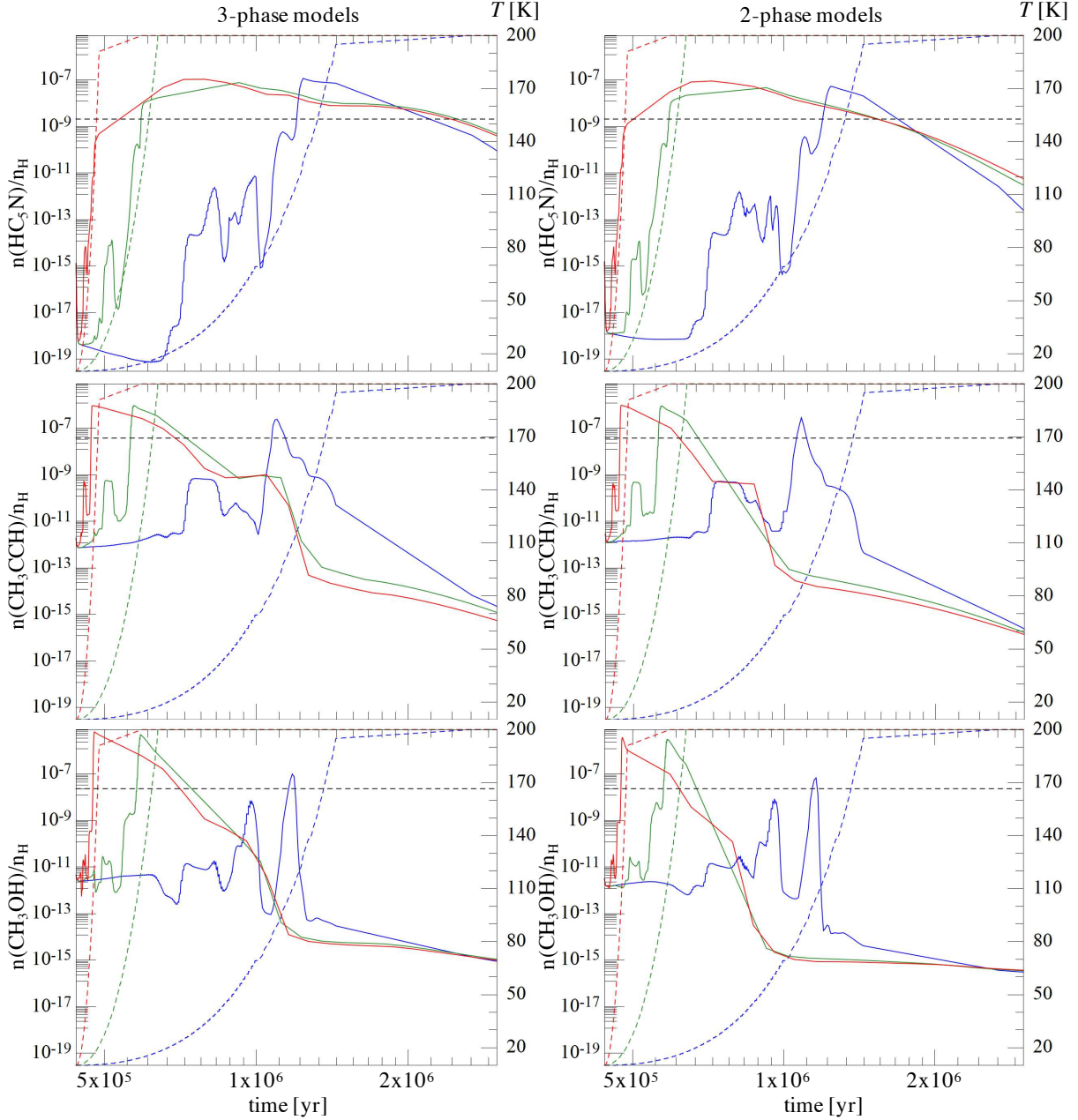


Figure 6. Comparisons between model results and lower limits derived for G28.28–0.36 (horizontal black dashed lines). The upper, middle, and lower panels show results for gas-phase HC_5N , CH_3CCH , and CH_3OH , respectively. The different colors of lines indicate different heating timescales; red, green, and blue indicate Fast, Medium, and Slow, respectively. The dashed curves indicate the temperature and their colors correspond to the heating timescales.

followed by



The CH_3CCH is subsequently adsorbed onto dust grains, in analogy with the cyanopolyynes, and starts to desorb at temperature of 70 K. The minimum temperature at which its lower limit observed in G28.28–0.36 ($3.8_{-2.2}^{+2.6} \times 10^{-8}$) is reproduced occurs only after its desorption from dust grains at ≈ 80 K, corresponding to ages of 4.7×10^5 yr, 5.6×10^5 yr, and 1.1×10^6 yr in the Fast, Medium, and Slow warm-up models, respectively. Its abundances decrease more rapidly compared to those of HC_5N , and the ranges of time which can reproduce the observed abundance become

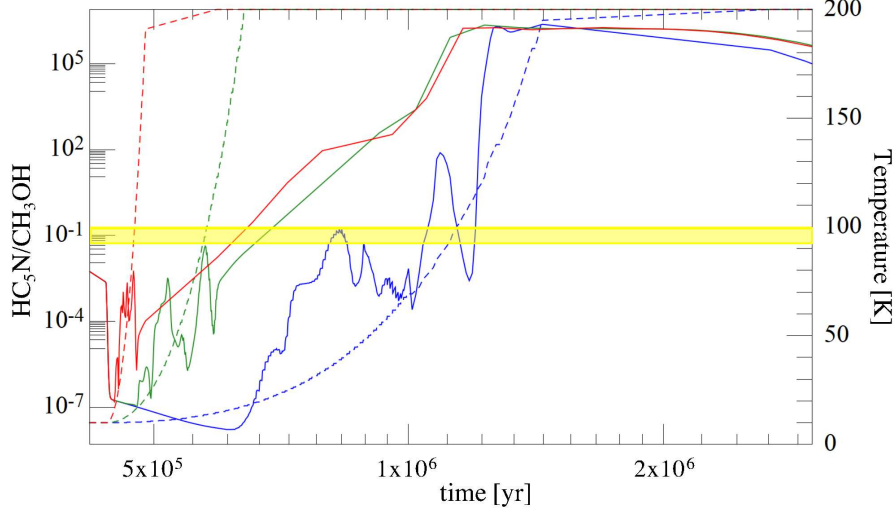


Figure 7. Temporal dependence of the $\text{HC}_5\text{N}/\text{CH}_3\text{OH}$ abundance ratio after the warm-up period. The different colors of lines indicate different heating timescales; red, green, and blue indicate Fast, Medium, and Slow, respectively. The dashed curves indicate the temperature and their colors correspond to the heating timescales. The yellow range corresponds to the value observed in the G28.28-0.36 ($0.091^{+0.109}_{-0.039}$).

narrower. Unlike HC_5N , CH_3CCH is destroyed by the reaction with atomic oxygen, leading to $\text{CO} + \text{C}_2\text{H}_4$. This reaction seems to contribute to the faster destruction of CH_3CCH .

The lower panels of Figure 6 show the results for CH_3OH , which is not a species produced by WCCC, because its sole production occurs on the grains via hydrogenation of CO. Nevertheless, its lower limit observed in G28.28-0.36 is also reproduced only after it desorbs into the gas phase at temperatures above ~ 100 K. The corresponding ages of the CH_3OH sublimation are 4.8×10^5 yr, 5.8×10^5 yr, and 1.1×10^6 yr in the Fast, Medium, and Slow warm-up models, respectively. Methanol is destroyed by reactions with ions such as HCO^+ .

In summary, the lower limits of all of these species derived in G28.28-0.36 can be reproduced only after desorption from dust grains. The observed species in G28.28-0.36 seem to reside in higher temperature regions when compared with WCCC sources. The HC_5N and CH_3OH abundances do not become higher than the observed abundances at the same age in the Slow warm-up models, although their peaks can be higher than the observed ones at different ages (Table 5).

We now return to a comparison of theory and observation concerning the abundance ratio of HC_5N to methanol in G28.28-0.36. The derived $N(\text{HC}_5\text{N})/N(\text{CH}_3\text{OH})$ column density ratio in G28.28-0.36 ($0.091^{+0.109}_{-0.039}$) is higher than that in the other three MYSOs by more than one order of magnitude (Taniguchi et al. 2018b). This ratio will be much lower in some HC_5N -undetected MYSOs than the HC_5N -detected MYSOs. In fact, Green et al. (2014) did not detect HC_5N in half of their target MYSOs.

Figure 7 shows temporal dependence of the $\text{HC}_5\text{N}/\text{CH}_3\text{OH}$ abundance ratio of Models M1 – M3. Because the individual abundances of both HC_5N and CH_3OH can be reproduced only after desorption from the gas, we investigated the ratio of their abundances only in this region. The actual investigated ranges of age are $4.75 \times 10^5 - 2.48 \times 10^6$ yr, $5.79 \times 10^5 - 1.02 \times 10^6$ yr, and $1.16 \times 10^6 - 1.3 \times 10^6$ yr for Models M1, M2, and M3, respectively. The closest calculated values to the observed ratios are ~ 0.20 at 6×10^5 yr ($T = 200$ K) in Model M1 and ~ 0.16 at 1.2×10^6 yr ($T \simeq 115$ K) in Model M3. In the case of Model M2, the calculated ratio with the current time resolution changes too rapidly and we could not find the exact value and age when the observed ratio is reproduced. From Figure 7, the observed ratio may be reproduced around 8×10^5 yr ($T = 200$ K) in Model M2. All of these ages correspond closely to the time when HC_5N reaches the peak abundances. These results may suggest that desorption of HC_5N or its further gas-phase formation have just started in hot regions in G28.28-0.36.

4.3. Effects of Cosmic Ray Ionization Rates on HC_5N Abundance

Fontani et al. (2017) suggested that a high cosmic-ray ionization rate of $\zeta \simeq 4 \times 10^{-14} \text{ s}^{-1}$ can reproduce their observational results for cyanopolyynes in OMC-2 FIR4. The observational results of the $c\text{-C}_3\text{H}_2$ abundance were also reproduced by such a high cosmic-ray ionization rate (Favre et al. 2018). In addition to runs with the common cosmic-

ray ionization rate of $\zeta = 1.3 \times 10^{-17} \text{ s}^{-1}$, we ran our models with high cosmic-ray ionization rates of $\zeta = 3.0 \times 10^{-16} \text{ s}^{-1}$ and $4.0 \times 10^{-14} \text{ s}^{-1}$, as Fontani et al. (2017) had done. Such high cosmic-ray ionization rates could be possible in protostellar systems (Padovani et al. 2016). Our results for gas-phase HC_5N abundances using these three ionization rates are shown in Figure 8. We used Models M3 and M1 with Slow and Fast warm-up timescales in panels (a) and (b), respectively.

In panel (a), the peak abundances decrease with an increase in the cosmic-ray ionization rate. This is caused by the fact that HC_5N is destroyed in the gas phase by reaction with H^+ and other ions before it is adsorbed onto dust grains. The H^+ ion destroys HC_5N most efficiently after $7 \times 10^5 \text{ yr}$:



This reaction is essential especially in the model with the cosmic-ray ionization rate of $4 \times 10^{-14} \text{ s}^{-1}$. The HC_5N^+ ion partly reacts with H_2 to form $\text{H}_2\text{C}_5\text{N}^+$, which contributes to re-formation of HC_5N through the electron dissociative recombination reaction. However, the reaction between HC_5N^+ and H_2 is much less effective compared to the electron dissociative recombination of HC_5N^+ to form C_5N and H , because the electron abundance becomes high in conditions with high cosmic-ray ionization rates. Polyatomic ions such as HCO^+ and H_3^+ react with electrons, leading to dissociative recombination, more rapidly than H^+ , and hence the relative abundance of H^+ to polyatomic ions becomes high. Thus, the H^+ becomes a reaction partner of HC_5N . In the model with the cosmic-ray ionization rate of $3.0 \times 10^{-16} \text{ s}^{-1}$, on the other hand, the HCO^+ ion is the main contributor to the destruction of HC_5N after 10^6 yr :



The formed $\text{H}_2\text{C}_5\text{N}^+$ will react with electrons and partly ($\sim 45 \%$) will go back to HC_5N . As discussed in the previous sections, the accumulation of HC_5N onto dust surface and in ice mantles is an important process in the slow warm-up models. However, the HC_5N destruction by ions works efficiently in the high cosmic-ray ionization models, and the accumulation of HC_5N is suppressed, leading to the lower HC_5N abundances. The HC_5N abundances in models with the two higher cosmic-ray ionization rates cannot reproduce its observed abundance in G28.28–0.36 even at peak abundance. However, there is no significant difference in peak abundance among the fast warm-up models with different cosmic-ray ionization rates in panel (b). With the highest cosmic-ray ionization rate, HC_5N continues to be formed by Reaction (11) efficiently, while the reaction is less efficient due to the significantly lower abundance of C_4H_2 in the models with the cosmic-ray ionization rate of $3.0 \times 10^{-16} \text{ s}^{-1}$ after $\sim 1 \times 10^6 \text{ yr}$. This highest cosmic-ray ionization model can reproduce the observed abundance in G28.28–0.36 for all times after $4.86 \times 10^5 \text{ yr}$ ($T \geq 170 \text{ K}$).

The HC_5N abundance in the slow warm-up model with cosmic-ray ionization rate of $4.0 \times 10^{-14} \text{ s}^{-1}$ is significantly lower than in the same cosmic-ray ionization rate model with fast warm-up. The difference between slow and fast warm-up models is caused by the different abundances of H^+ and H_3^+ , which in turn are related to the abundances of H and H_2 . In the slow warm-up model, the H_2 formation rate is slowed down by an exponential factor of the form $\exp(-\frac{E_{\text{diff}}}{T})$, where E_{diff} is known as the diffusion barrier and T is the temperature. The diffusion barrier slows the average motion of the reacting hydrogen atoms. The destruction rate of H_2 is larger than its formation rate in such a high cosmic-ray ionization condition. The retarding effect of the diffusion barrier is lessened in the fast warm-up model because of the higher temperatures even at early times. Hence, the H abundance is higher than that of H_2 in the slow warm-up model, while the H_2 abundance is higher in the fast warm-up model. In the slow warm-up model, the H^+ ion is efficiently formed by the ionization of H atom by cosmic rays. On the other hand, in the fast warm-up model, the H^+ ion is formed by the reaction between H_2 and cosmic rays, leading to H , H^+ , and electrons, which is slower than the ionization of H atoms by cosmic rays. Hence, the formation of the H^+ ion is more efficient in the slow warm-up model. Cosmic rays also produce H_2^+ from H_2 ionization. The H_2^+ ion subsequently reacts with H_2 forming the H_3^+ ion in the fast warm-up model, whereas H_2^+ reacts with H to form H_2 and H^+ in the slow warm-up model. Therefore, in the slow warm-up model, the H^+ abundance is larger than that of H_3^+ , while the opposite is true in the fast warm-up model.

The H^+ ion contributes to destruction of HC_5N to form HC_5N^+ in the slow warm-up model. The reaction between HC_5N^+ and electrons cannot produce HC_5N . In the fast warm-up model, on the other hand, the reactions with H_3^+ and HCO^+ destroy HC_5N , and both reactions form $\text{H}_2\text{C}_5\text{N}^+$, which reacts with electron and partially goes back to HC_5N . Reaction (11) continues to form HC_5N in both models and this reaction is particularly important for the slow warm-up model. The C_4H_2 molecules are formed from large hydrocarbons (e.g., C_4H) and their ions (e.g., C_4H_3^+) in

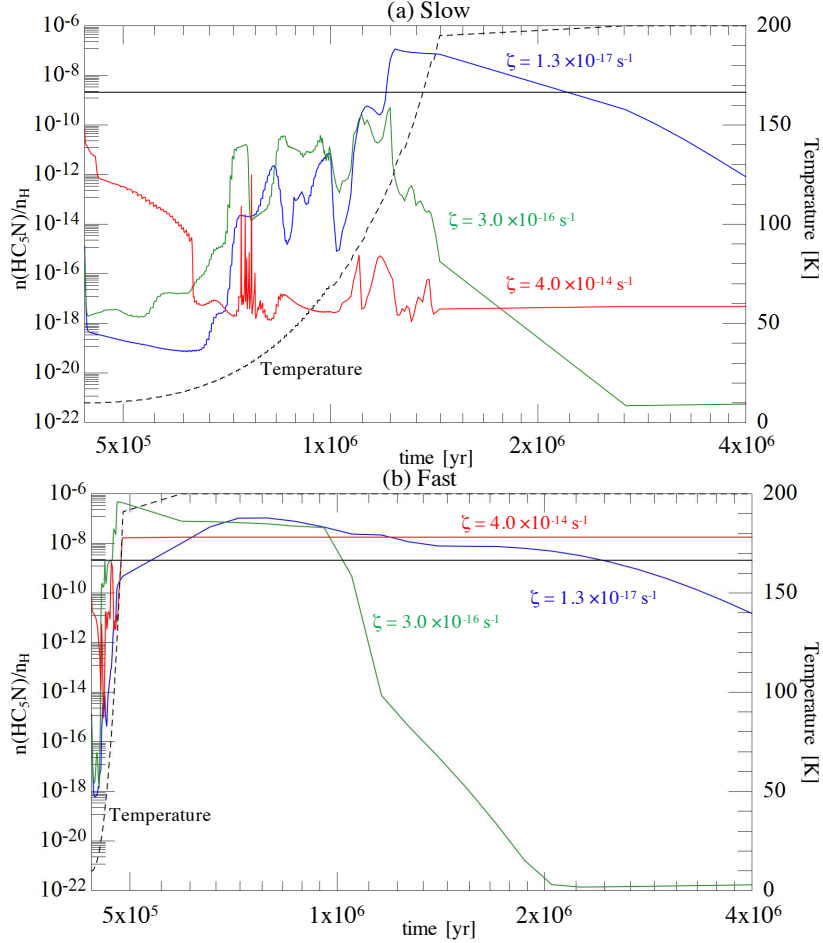


Figure 8. HC_5N abundances calculated with 3-phase models during the warm-up period. Panels (a) and (b) show the results using the Slow (M3) and Fast (M1) heating timescales, respectively. The different colors of lines indicate different cosmic-ray ionization rates: blue, green, and red indicate 1.3×10^{-17} , 3.0×10^{-16} , and $4.0 \times 10^{-14} \text{ s}^{-1}$, respectively. The black dashed curves indicate the temperature. The horizontal black lines indicate the lower limit of the observed abundance in G28.28–0.36.

both models, not bottom-up formation starting from CH_4 . Therefore, the carbon-chain formation starting from CH_4 is no longer an important formation mechanism of cyanopolyynes for the highest cosmic-ray ionization models.

In summary, the lower limit of HC_5N observed in the G28.28–0.36 MYSO can be reproduced with temperatures above $\sim 115 \text{ K}$ in all of the models with the typical cosmic-ray ionization rate of $1.3 \times 10^{-17} \text{ s}^{-1}$. In the case of the Slow warm-up timescale, the models with high cosmic-ray ionization rates cannot reproduce the observed abundance of HC_5N in G28.28–0.36. On the other hand, the model with Fast warm-up timescale and the highest cosmic-ray ionization rate can maintain the high abundance of HC_5N .

4.4. Comparisons among Carbon-Chain Species

We found unusual features of the cyanopolyynes during the warm-up period; in particular, they are formed initially in the gas phase, subsequently accumulate in the bulk of the icy mantle, and then desorb into the gas phase, with their gas-phase peak abundances attained when they desorb. The carbon-chain molecule CH_3CCH shows a similar feature (Section 4.2).

Figure 9 shows the abundances of CCH (red), CCS (green), and $c\text{-C}_3\text{H}_2$ (blue) during the warm-up period. The species CCH and CCS show abundance peaks just after the temperature rises to 25 K. The CCH molecule is efficiently destroyed by the reaction with atomic oxygen (O) during $1.0 \times 10^6 \leq t \leq 1.07 \times 10^6 \text{ yr}$, when the temperature rises from $\sim 70 \text{ K}$ to $\sim 80 \text{ K}$. The subsequent decrease in the gas-phase CCH abundance is caused by its efficient destruction by reaction with H_2 , which occurs efficiently with the temperature of $\geq 90 \text{ K}$, at a time of $t \geq 1.1 \times 10^6 \text{ yr}$ (Hassel et al. 2011). Dicarbon sulfide, or CCS, is destroyed by the reaction with atomic oxygen (O). The atomic oxygen desorbs at

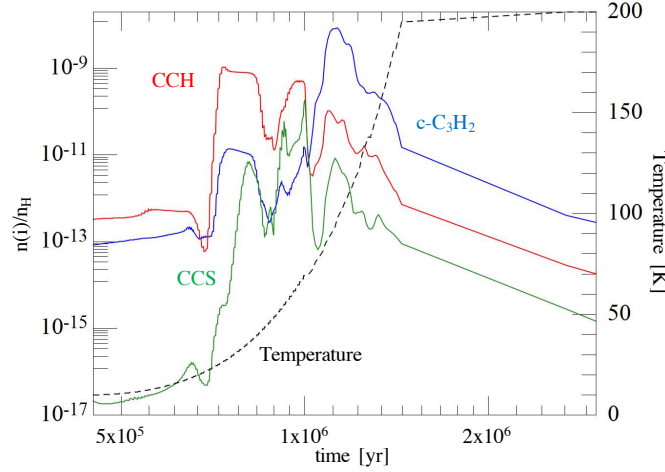
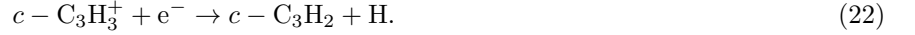


Figure 9. Abundances of carbon-chain species in the gas phase during the warm-up period (Model M3). The red, green, and blue curves indicate results for CCH, CCS, and $c\text{-C}_3\text{H}_2$, respectively. The black dashed line indicates temperature.

temperatures above 60 K (He et al. 2015) at a time of $t \geq 1.0 \times 10^6$ yr. Because of these rapid gas-phase reactions, desorption from dust surfaces is not important for the synthesis of gas-phase CCH and CCS.

On the other hand, $c\text{-C}_3\text{H}_2$ shows its gas-phase peak abundance after its direct evaporation from the dust surface at temperatures above 90 K at a time of $t \geq 1.1 \times 10^6$ yr, as is the case for the cyanopolyynes and CH_3CCH . The cyclic species $c\text{-C}_3\text{H}_2$ is produced in the gas-phase both in the pre-warm-up period and during the warm-up period starting with the sublimation of CH_4 . The main formation pathway of $c\text{-C}_3\text{H}_2$ is the dissociative recombination reaction of $c\text{-C}_3\text{H}_3^+$:



Gaseous $c\text{-C}_3\text{H}_2$, formed in the low-temperature portion of the warm-up period, is subsequently adsorbed onto dust grains, from which it desorbs after $\sim 1.0 \times 10^6$ yr at temperatures $T \geq 65$ K. It is efficiently destroyed by the reaction with H_2 at temperatures above 120 K ($t \geq 1.2 \times 10^6$ yr). Hence, the efficient destruction of $c\text{-C}_3\text{H}_2$ occurs after it desorbs. All species in Figure 9 decrease in abundance with parallel curves after 1.5×10^6 yr.

In summary, there are largely two types of carbon-chain species in warm-up regions. One type shows peak abundances just after their desorption from dust grains; these include cyanopolyynes, CH_3CCH , and $c\text{-C}_3\text{H}_2$. The other type shows peak abundances just after the temperature rises to 25 K (CCH and CCS). The latter include relatively reactive species, which are easily destroyed in the gas phase. On the other hand, cyanopolyynes are not destroyed by reactions with H_2 and O, but react with ions such as H^+ , H_3^+ , and HCO^+ , and so eventually decrease.

Such differences among carbon-chain species seem to explain the observational results in HMPOs (Taniguchi et al. 2018c, 2019) and massive cluster-forming regions (Shimoikura et al. 2018). Taniguchi et al. (2018c) suggested that HC_3N is newly formed in the warm and well-shielded dense gas around HMPOs, and Taniguchi et al. (2019) reported that the detection rates for the cyanopolyynes, defined by the number of sources where target molecules were detected divided by the number of total observed sources $\times 100$, are higher around HMPOs than in low-mass protostars, but that of CCS is lower. Shimoikura et al. (2018) concluded that HC_3N tends to be abundant, whereas CCS detection is rare in massive cluster-forming clumps, where it has probably been already destroyed by reaction with O because the dust temperature should be higher than the sublimation temperature of atomic oxygen. On the other hand, HC_3N can still be abundant in such high temperature regions.

4.5. Implication for Chemical Diversity around Massive Young Stellar Objects (MYSOs)

As already mentioned in Section 1, the different timescales of the starless core phase (Sakai & Yamamoto 2013) and the penetration of the interstellar radiation field (Spezzano et al. 2016) were proposed as possible origins of chemical diversity in low-mass star-forming regions. High-mass stars are usually born in giant molecular clouds (GMCs), and there is a possibility that the formation of high-mass starless cores starts long after the clouds were well shielded against the interstellar radiation field unless GMCs have clumpy structures. In the former case, there should be enough time for atomic carbon to convert into CO molecules. In particular, the interstellar radiation field may be important for the outer edge of GMCs but not for the inner regions, as is the well-known case of photon-dominated regions (PDRs).

Chemical diversity can also be caused by the dependence of abundance on the heating rate. For example, CH_3OH shows higher peak abundances in those models with a Fast heating timescale. On the other hand, as discussed above, HC_5N tends to be more abundant in the models with the Slow heating timescale because there is enough time for HC_5N to accumulate in the bulk of the icy mantle before desorption. This may be one possible origin of the chemical diversity around MYSOs (Taniguchi et al. 2017, 2018b).

The heating timescale of warm-up regions depends not only on stellar masses but also on the relationship between the size of the warming region and the infall velocity (Aikawa et al. 2008) as given by

$$t_h \propto \frac{R_{\text{warm}}}{V_{\text{infall}}}, \quad (23)$$

where t_h , R_{warm} , and V_{infall} are the heating timescale, the size of the warm region, and the infall velocity, respectively. If R_{warm} becomes larger or V_{infall} becomes smaller, t_h will be longer. Such a condition will lead to HC_5N -rich/ CH_3OH -poor envelopes around MYSOs, which is similar to the case of G28.28–0.36.

The size of warm regions and their infall velocity relate to other physical conditions. For example, the size of warm regions depends upon the luminosity of the central stars, and the density structure (Nomura & Millar 2004), while the infall velocity is related to the density, rotating motion, magnetic field, and radiation pressure (e.g., Sugiyama et al. 2014). Consequently, the heating timescale is also related to the physical conditions in star-forming regions. Observations investigating relationships between the chemical diversity and Equation (23) are necessary to constrain the proposed scenario.

The possibility of UV radiation to cause chemical diversity should be considered in cluster regions. The first born star should affect its environment and the strong UV radiation it emits can destroy CO molecules to form C and/or C^+ , which will be precursors of carbon-chain species. In that case, we would expect chemical diversity among sources in the same cluster region. As discussed in Section 4.3, the cosmic-ray ionization rate significantly affects the abundances of cyanopolyynes. Cosmic rays can penetrate deeper dense regions compared to the UV radiation. Hence, the effects of cosmic rays may be essential particular in the dense cores including hot cores.

The binding energies are affected by significant errors (Table 6 in Appendix A) and they change with ice-mantle surface composition (e.g., Nguyen et al. 2018). More laboratory work should be dedicated to binding energy measurements; meanwhile, detailed comparison between model predictions and observational results toward star-forming regions will help to put constraints on these important parameters.

5. CONCLUSIONS

We have investigated cyanopolyynne chemistry around MYSOs with warm-up hot-core models using the Nautilus code, and motivated by recent observational results toward MYSOs (Taniguchi et al. 2017, 2018b). The main conclusions of this paper are as follows:

1. Cyanopolyynes are formed via neutral-neutral and ion-neutral reactions in the lukewarm gas ($25 < T < 100$ K). The sublimation of CH_4 and C_{2n}H_2 from dust grains enhances key reactions for the formation of cyanopolyynes. They are simultaneously accumulated on the dust surface and in the bulk of icy mantles in this temperature range. Cyanopolyynes sublime into the gas phase when the temperature rises above ~ 100 K and reach their peak abundances in the gas phase.
2. The carbon chain CH_3CCH shows similar characteristics to cyanopolyynes. It is formed from CH_4 sublimated from dust grains and accumulates onto dust grains before the temperature reaches its sublimation temperature of 70 K. After the temperature reaches 70 K, CH_3CCH desorbs from dust grains and shows the gas-phase peak abundance.
3. Models with a longer warm-up period enable these species to accumulate to a greater extent in the bulk of icy mantles.
4. Our model results can reproduce the lower limits of HC_5N , CH_3CCH , and CH_3OH observed in the G28.28–0.36 MYSO, where HC_5N is particularly abundant (Taniguchi et al. 2017). Their observed abundances are reproduced best just after their sublimation from dust grains.
5. The species CCH and CCS show their peak abundances just after they are formed in the gas phase triggered by the evaporation of CH_4 . The chemistry that produces them is the WCCC chemistry. They are reactive

species and destroyed by H_2 or O in the gas phase. On the other hand, cyanopolyynes, CH_3CCH , and $c\text{-C}_3\text{H}_2$ are relatively stable species and can accumulate in the bulk of icy mantles before destruction in the gas phase. This implies that there are largely two types of carbon-chain species. Such results seem to explain the higher detection rates of cyanopolyynes than that of CCS in HMPOs and cluster-forming regions.

6. HC_5N -rich and CH_3OH -poor envelopes around MYSOs may reflect different heating timescales. The heating timescale depends not only on the mass of central stars but also on the relationships between the size of warm regions and their infall velocity, which in turn relate to various physical conditions, including luminosity, density, magnetic field, rotating motion, and radiation pressure.

K. T. would like to thank the University of Virginia for providing the funds for her postdoctoral fellowship in the Virginia Initiative on Cosmic Origins (VICO) research program. E. H. is grateful for support from the National Science Foundation through grant 1514844.

Software: Nautilus (Ruard et al. 2016)

APPENDIX

A. BINDING ENERGY

Table 6 summarizes binding energies of major species and key species in this paper utilized in our model. These binding energy values and errors are taken from the KIDA database (Wakelam et al. 2017).

Table 6. Binding energies of major species

Species	Binding Energy (K)	Species	Binding Energy (K)
H	650 ± 195	C_2H_2	2587 ± 776
H_2	440 ± 132	C_4H_2	4187
C	4000	C_6H_2	5787
O	1660 ± 60	HC_3N	4580
N	800	HC_5N	6180
CO	1150	HC_7N	7780
CN	1600	CH_3OH	5534
CH_4	1300	CH_3CCH	4287

NOTE—These values are applied for species on amorphous water ice surface (Wakelam et al. 2017).

REFERENCES

- Acharyya, K., & Herbst, E. 2017, *ApJ*, 850, 105
- Aikawa, Y., Wakelam, V., Garrod, R. T., & Herbst, E. 2008, *ApJ*, 674, 984
- Balucani, N., Ceccarelli, C., & Taquet, V. 2015, *MNRAS*, 449, L16
- Belloche, A., Müller, H. S. P., Menten, K. M., Schilke, P., & Comito, C. 2013, *A&A*, 559, A47
- Benson, P. J., Caselli, P., & Myers, P. C. 1998, *ApJ*, 506, 743
- Bergantini, A., Góbi, S., Abplanalp, M. J., & Kaiser, R. I. 2018, *ApJ*, 852, 70
- Beuther, H., Schilke, P., Menten, K. M., et al. 2002, *ApJ*, 566, 945
- Bonfand, M., Belloche, A., Menten, K. M., Garrod, R. T., & Müller, H. S. P. 2017, *A&A*, 604, A60
- Burkhardt, A. M., Herbst, E., Kalenskii, S. V., et al. 2018, *MNRAS*, 474, 5068
- Caselli, P., & Ceccarelli, C. 2012, *A&A Rv*, 20, 56
- Esplugues, G. B., Cernicharo, J., Viti, S., et al. 2013, *A&A*, 559, A51
- Favre, C., Ceccarelli, C., López-Sepulcre, A., et al. 2018, *ApJ*, 859, 136

- Fontani, F., Ceccarelli, C., Favre, C., et al. 2017, *A&A*, 605, A57
- Garrod, R. T. 2013, *ApJ*, 765, 60
- Garrod, R. T., & Herbst, E. 2006, *A&A*, 457, 927
- Green, C.-E., Green, J. A., Burton, M. G., et al. 2014, *MNRAS*, 443, 2252
- Hassel, G. E., Harada, N., & Herbst, E. 2011, *ApJ*, 743, 182
- Hassel, G. E., Herbst, E., & Garrod, R. T. 2008, *ApJ*, 681, 1385
- He, J., Shi, J., Hopkins, T., et al. 2015, *ApJ*, 801, 120
- Herbst E. & Millar, T. J. 2008, in *Low Temperatures and Cold Molecules*, Smith, I. W. M. ed. (London: Imperial College Press), p. 1
- Herbst, E., & van Dishoeck, E. F. 2009, *ARA&A*, 47, 427
- Hirota, T., Ohishi, M., & Yamamoto, S. 2009, *ApJ*, 699, 585
- Hudson, R. L., & Moore, M. H. 2018, *ApJ*, 857, 89
- Jaber Al-Edhari, A., Ceccarelli, C., Kahane, C., et al. 2017, *A&A*, 597, A40
- Jørgensen, J. K., Schöier, F. L., & van Dishoeck, E. F. 2002, *A&A*, 389, 908
- Lee, H.-H., Herbst, E., Pineau des Forets, G., Roueff, E., & Le Boulart, J. 1996, *A&A*, 311, 690
- Li, X., Heays, A. N., Visser, R., et al. 2013, *A&A*, 555, A14
- McGuire, B. A., Burkhardt, A. M., Kalenskii, S., et al. 2018, *Science*, 359, 202
- Nguyen, T., Baouche, S., Congiu, E., et al. 2018, *A&A*, 619, A111
- Nomura, H., & Millar, T. J. 2004, *A&A*, 414, 409
- Padovani, M., Marcowith, A., Hennebelle, P., & Ferrière, K. 2016, *A&A*, 590, A8
- Reboussin, L., Wakelam, V., Guilloteau, S., & Hersant, F. 2014, *MNRAS*, 440, 3557
- Ruaud, M., Wakelam, V., & Hersant, F. 2016, *MNRAS*, 459, 3756
- Sakai, N., Sakai, T., Hirota, T., Burton, M., & Yamamoto, S. 2009, *ApJ*, 697, 769
- Sakai, N., Sakai, T., Hirota, T., & Yamamoto, S. 2008, *ApJ*, 672, 371
- Sakai, N., & Yamamoto, S. 2013, *Chemical Reviews*, 113, 8981
- Shimoikura, T., Dobashi, K., Nakamura, F., Matsumoto, T., & Hirota, T. 2018, *ApJ*, 855, 45
- Shingledecker, C. N., & Herbst, E. 2018, *Physical Chemistry Chemical Physics (Incorporating Faraday Transactions)*, 20, 5359
- Skouteris, D., Balucani, N., Ceccarelli, C., et al. 2018, *ApJ*, 854, 135
- Spezzano, S., Bizzocchi, L., Caselli, P., Harju, J., & Brünken, S. 2016, *A&A*, 592, L11
- Sugiyama, K., Fujisawa, K., Doi, A., et al. 2014, *A&A*, 562, A82
- Suzuki, H., Yamamoto, S., Ohishi, M., et al. 1992, *ApJ*, 392, 551
- Taniguchi, K., Miyamoto, Y., Saito, M., et al. 2018a, *ApJ*, 866, 32
- Taniguchi, K., Ozeki, H., Saito, M., et al. 2016a, *ApJ*, 817, 147
- Taniguchi, K., & Saito, M. 2017, *PASJ*, 69, L7
- Taniguchi, K., Saito, M., Hirota, T., et al. 2017, *ApJ*, 844, 68
- Taniguchi, K., Saito, M., Majumdar, L., et al. 2018b, *ApJ*, 866, 150
- Taniguchi, K., Saito, M., & Ozeki, H. 2016b, *ApJ*, 830, 106
- Taniguchi, K., Saito, M., Sridharan, T. K., & Minamidani, T. 2018c, *ApJ*, 854, 133
- Taniguchi, K., Saito, M., Sridharan, T. K., & Minamidani, T. 2019, *ApJ*, 872, 154
- van Dishoeck, E. F. 2018, *IAU Symposium*, 332, 3
- Visser, R., van Dishoeck, E. F., & Black, J. H. 2009, *A&A*, 503, 323
- Viti, S., Collings, M. P., Dever, J. W., McCoustra, M. R. S., & Williams, D. A. 2004, *MNRAS*, 354, 1141
- Wakelam, V., Loison, J.-C., Mereau, R., & Ruaud, M. 2017, *Molecular Astrophysics*, 6, 22